Thermoelectric Properties of Doped Silicon Nanocrystal Films Deposited by Nonthermal Plasmas

A THESIS

SUBMITTED TO THE FACULTY OF THE

UNIVERSITY OF MINNESOTA

BY

Yueke Yang

IN PARTIAL FULFULLMENT OF THE REQUIRMENTS

FOR THE DEGREE OF

MASTER OF SCIENCE

Prof. Uwe R. Kortshagen, Advisor

June 2019

Acknowledgements

I want to thank a lot of people for helping and supporting me in my life to where I am today. First, I would like to thank my Grandpa, Dad, and Mom, who always encourage me, stand with me, and support me to pursue what I want to do. Thank you to my advisor, Prof. Kortshagen, who provides a chance to do scientific researches in the past two and a half years and gives me many suggestions. Thank you to Prof. Kakalios, who lets me use his lab instrument to complete experiments and guides me on how to deal with research problems. To my friends in the lab, thank you Katelyn for training me at the beginning of my graduate school journey, thank you Kelsey, Katharine, Sadhana, and Ali for helping and guiding me on my experiments, and thank you Bo in Chemistry Department for completing a project together, thank you everyone in the group for listening to my presentations, sharing your knowledge, and providing many useful suggestions. To my friends outside the lab, a long list of people, thank you for your help and leave so many beautiful moments.

Table of Contents

List of Tables

List of Figures

1. Introduction

1.1 Background

Energy demand has become the focus of attention in the whole world in the past several decades as remaining non-renewable energy resources such as petroleum, coal, and natural gas decrease rapidly. To address this problem, thousands of experts and researchers have spent billions of dollars on studying and developing renewable energy resources such as solar energy, nuclear energy, and thermal energy. Among these renewable energy resources, thermal energy is arguably the most significant and indispensable one due to the fact that two-thirds of all created energy is lost as heat.[1] Even though not all of them can be used again, there is additional heat energy lost that could be recovered. Additionally, environmental problems such as global warming, caused by the combustion of fossil fuels, are becoming increasingly aggravated. Therefore, studying and using high-performance, environmentally friendly and inexpensive thermoelectric materials to achieve efficient conversion from waste heat to electrical energy is momentous and imperative.

1.2 Thermoelectric performance of silicon

Each thermoelectric device consists of N-type and P-type materials shown in Figure 1.1. For the P-type materials, the main carriers are holes. For the N-type materials, the main carriers are electrons. The temperatures of two sides are different. There are more carriers at the hot side than cold side to form a voltage difference between them. Therefore, the device can generate the current through this voltage difference.

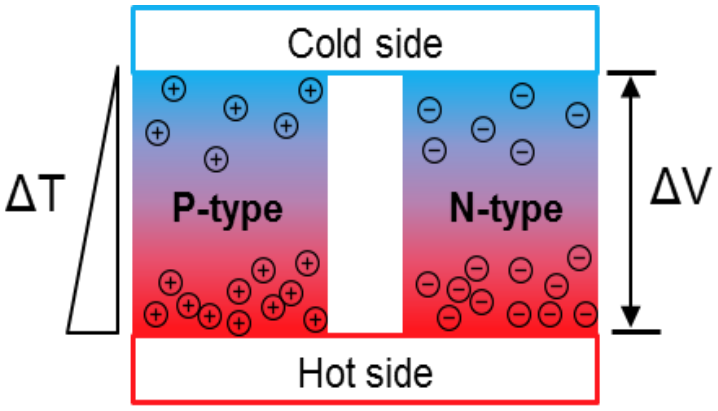

Figure 1.1. Electron kinetics within a thermoelectric module.

The thermoelectric performance of a device is usually evaluated by its efficiency (η), which can be expressed as:

$$\eta = \frac{T_H - T_C}{T_H}\left[\frac{(1+ZT)^{1/2}-1}{(1+TZ)^{1/2}+(T_C/T_H)}\right] \quad (1)$$

where T_C and T_H are the temperature of the cold and hot site. From equation (1), the thermoelectric efficiency depends crucially on the thermoelectric figure of merit (ZT), which is related to the electrical conductivity(σ), Seebeck coefficient (S), the thermal conductivity due to electrons (κ_e), the lattice thermal conductivity due to phonons (κ_l), and the absolute temperature (T), as shown in equation (2). Specifically, better thermoelectric performance is achieved at higher ZT values. Simulation results visualizing the dependence of η and temperature difference are shown in Figure 1.2

$$ZT = \frac{\sigma S^2 T}{\kappa_e + \kappa_l} \quad (2)$$

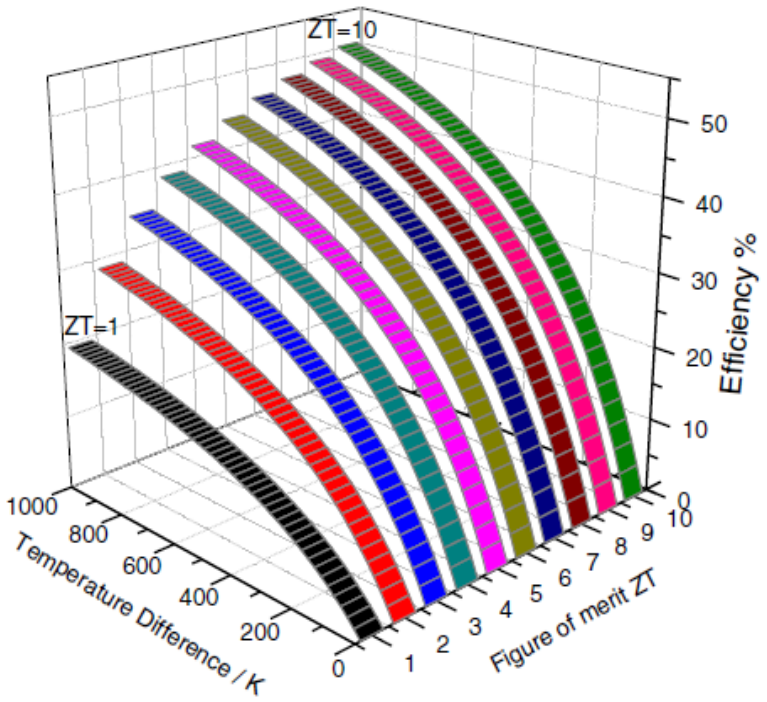

Figure 1.2. Simulation results of the dependence of the thermoelectric efficiency on figure of merit (ZT) and temperature difference. [2]

Depending on the desired scale of power generation, two different directions are explored for thermoelectric devices. For the large power case, researchers try to obtain a high ZT to achieve the maximum thermoelectric efficiency. For the small power case, device voltage is more significant, requiring a high Seebeck coefficient and a reasonable electrical conductivity.[3] High efficiencies have been found in materials like PbTe,[1] conjugated polymer,[3] Bi_2Te_3,[4] Cu_2S,[5] skutterudites,[6] Zintl,[7] and clathrates.[8] Among these materials, Bi_2Te_3 was the first promising thermoelectric material that had been studied,[9] and the alloy of Bi_2Te_3 and Sb_2Te_3 are now widely used due to their high figures of merit. For example, n-doped $Bi_2Te_3/Bi_2Te_{2.83}Sb_{0.17}$ superlattice shows ZT around 1.4 and p-doped Bi_2Te_3/Sb_2Te_3 superlattice shows ZT up to around 2.4 at room temperature, as shown by Venkatasubramanian et al..[4]

Although Bi_2Te_3 and Sb_2Te_3 are promising and attractive thermoelectric materials and have been studied for decades due to their high ZT values, the high costs make it challenging to apply them in practical thermoelectric devices. Therefore, a low-cost and high-yield material with promising high thermoelectric performance is needed. Silicon is one of the most abundant and widely used environmentally friendly semiconductor materials in the world. However, in its bulk form, silicon has high thermal conductivities on the level of 150 $Wm^{-1}K^{-1}$ at room temperature,[10] leading to low ZT values around 0.01 at 300 K unsuitable for thermoelectric applications.[11] Since the 1990s, there has been a resurged interest in studying thermoelectric materials as it was theoretically predicted that thermoelectric efficiency can be improved significantly through nanostructuring.[12] Since then, an increase in literature that discusses the thermoelectric properties of porous silicon has been observed.[13]-[20] Nanostructuring of silicon has been studied because it was found to decrease the thermal conductivity without proportionally reducing the power factor ($PF = \sigma S^2$). Altering the nanostructures can result in grain sizes much smaller than the mean free path of the phonons to reduce the thermal conductivity significantly, while still larger than the mean free path of the electrons and holes, which does not affect the electron or hole transport significantly. To sum up, this decreases the σ/κ while S is kept somewhat constant and a higher ZT is achieved.[21] For example, ZTs of up to 1 have been found in silicon nanowires by reducing the thermal conductivity to around 1.6 $Wm^{-1}K^{-1}$ without changing the power factor significantly.[13], [14] Porous silicon shows ZT around 0.4 at room temperature, which is also much higher than the bulk silicon.[22]

1.3 Nonthermal plasma method

In the literature, many kinds of methods like thermal,[23] laser pyrolysis,[24] superlattice nanowire pattern transfer (SNAP),[13] low pressure chemical vapor deposition (LPCVD) and etching,[15] deep reactive ion etching (DRIE),[17] PECVD,[25] and nonthermal plasma synthesis[26] were used to synthesize silicon with different nanostructures. In this paper, we propose to deposit doped silicon nanocrystal thin films via nonthermal plasma synthesis.

Nonthermal plasma synthesis is a viable alternative technology in the liquid or gas phase methods to synthesize high purity nanocrystal materials which require high synthesis temperature to be produced in crystalline form.[27] This technique emerged around twenty years ago for producing high-quality semiconductor nanocrystals. In 1997, spherical Si NCs and Ge NCs were produced with the inductively-coupled radio frequency (RF) plasma by Gorla et al..[28] Mangolini, Thimsen, and Kortshagen showed a capacitively-coupled RF plasma reactor to control the size, shape, and mono-dispersion of NCs in 2005.[26] Compared with other methods, nonthermal plasma synthesis method has these advantages[27]: high-purity nanocrystals without solvents and ligands, narrow size distribution of nanocrystals, controllable and efficient doping, and low gas temperature. However, to achieve the wild applications of these nanomaterials, such as solar cells, gas sensors, and thermoelectrical device, after obtaining controllable NCs, it is quite significant to produce dense thin films consists of these NCs. Therefore, in 2010, Holman and Kortshagen introduced a new, flexible technique to synthesize dense Ge NC thin film with roll-to-roll process.[29]

1.4 Motivation

In this research, phosphorus doped and boron doped silicon nanocrystal films were synthesized using nonthermal plasma with roll-to-roll process.[29] SEM and XRD were used to characterize these films. Electrical conductivities and Seebeck coefficients of these films were measured at the different temperatures in the vacuum chamber. The effect of doping level, annealing, thickness, and oxidation on electrical conductivities and Seebeck coefficients were studied and discussed to improve the thermoelectric performance.

2. Phosphorus-doped silicon nanocrystal films

2.1 Background

For each thermoelectric device, it needs both P-type and N-type materials, which have the similar coefficient of thermal expansion. This research focus on studying phosphorus-doped silicon nanocrystals (P-doped Si NCs) as the N-type material, and boron-doped silicon nanocrystals (B-doped Si NCs) as the P-type material.

In this chapter, some studies of thermoelectrical properties of P-doped Si NCs are shown. First, synthesis parameters to affect the density of films were studied. Dense films is the base to study the thermoelectric properties of films. Then, the relationship between the electrical conductivity and the temperature in different phosphorus doping level Si NC films were shown. Finally, the effect of annealing in the glovebox, thickness, and oxidation on the electrical conductivity and Seebeck coefficient of P-doped films were studied. A probable mechanism was found to explain the abnormal Seebeck coefficient change.

2.2 Experimental methods

In this research, both P-doped Si NC films and B-doped Si NC films were synthesized in nonthermal plasma reactor shown in Figure 2.1. Before synthesis, N_2 was used to purge the reactor three times and basic pressure was pumped down lower than 20 mTorr. The leak rate was smaller than 8 mTorr/min. For the P-doped Si NC films, SiH_4 and PH_3 as precursors were injected into the quartz tube with Ar as the carrier gas. Two copper electrodes generated the nonthermal plasma with an Advanced Energy RFX 600 Radio

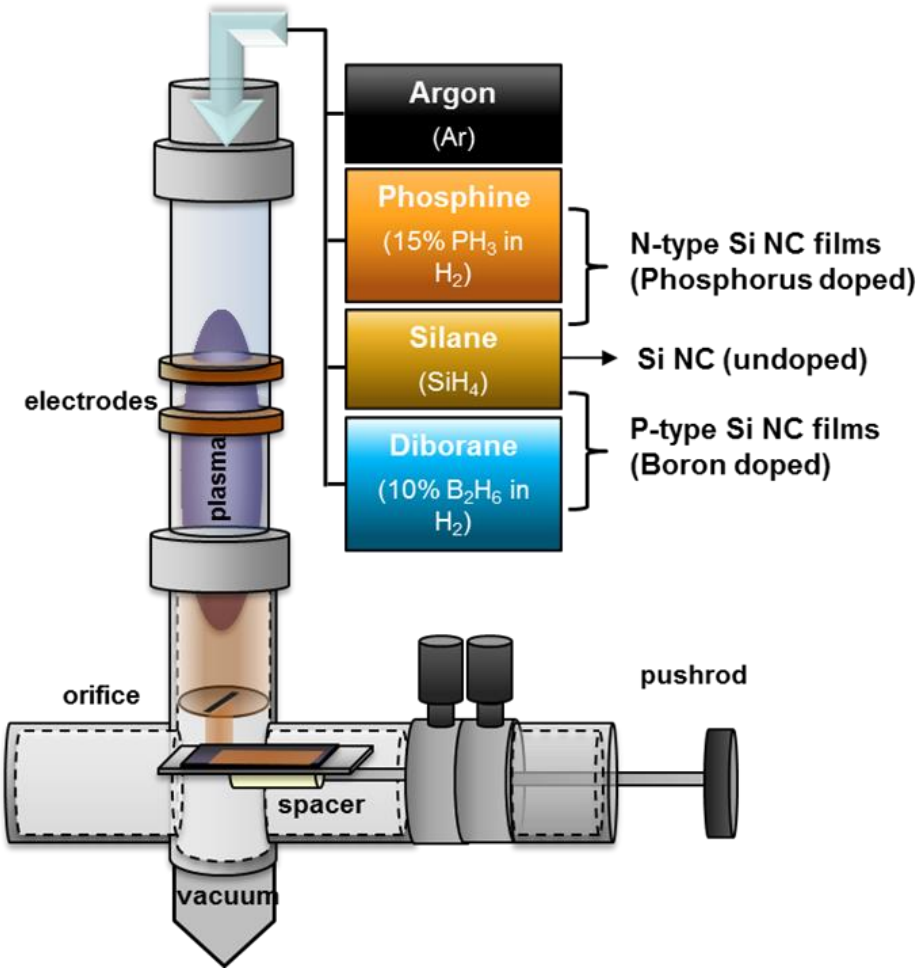

Figure 2.1 Schematic of the plasma reactor. Continuous mixed gases forms NCs in the plasma and pass through the orifice to deposit a film on the substrate. [30]

Frequency power supply at 13.56 MHz. Output power was 110 W. The upstream pressure, the pressure above the orifice in the tube was 4 Torr to 5 Torr during the synthesis. Precursors dissociated and nucleated in the plasma. Then, nanocrystals were generated and accelerated through an orifice with an adjustable slit and deposited onto the substrate attached to the pushrod. During the synthesis, the pushrod was moved forward and backward to get the smooth film.

Due to the dangerous nature of precursors, PH_3 is diluted 15% in H_2 and B_2H_6 was diluted 10% H_2 to reduce potential exposure concentrations.[30]

Table 2.1 Process gases used in this work.[30]

	Gas composition	Structure	Symbol	Toxic hazard	Fire hazard
Silane	100%	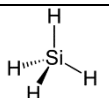	SiH_4	Slightly	Yes
Phosphine	15% in Hydrogen	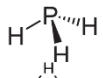	PH_3	Yes	Yes
Diborane	10% in Hydrogen	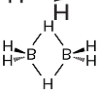	B_2H_6	Yes	Yes
Argon	100%		Ar	In high levels	No
Hydrogen	n/a		H_2	Low	Yes

The properties of gases in this work are shown in Table 2.1.

Scanning Electron Microscopy (SEM): SEM images were obtained by a field emission gun scanning electron microscopy JEOL 6500 with the accelerating voltage 5 kV and working distance around 10 mm.

X-ray Diffraction Diffreaction (XRD): The crystalline diffraction pattern was characterized by X-ray diffraction by using a Bruker D8 Discover 2D with a 2.2 kW sealed Cu X-ray source at the room temperature in the air.

Annealing in the N_2 glovebox: Samples were annealed on the heater at 450 $^{\circ}$C for 1 h in the N_2 glovebox. Both the O_2 level and H_2O level in the N_2 glovebox were controlled less than 0.1 ppm to reduce the effect of the oxidation.

Current-voltage measurement: The sample was placed across two copper blocks with heaters as shown in Figure 2.2. The current-voltage (I-V) characteristics of doped Si NC films were measured in the dark and vacuum chamber by Keithley model 617 programmable electrometer and homemade LabVIEW programs at different temperature from 300 K to 400 K by Lakeshore 336 temperature controller with a fixed ramp rate of 2.5 K/min.

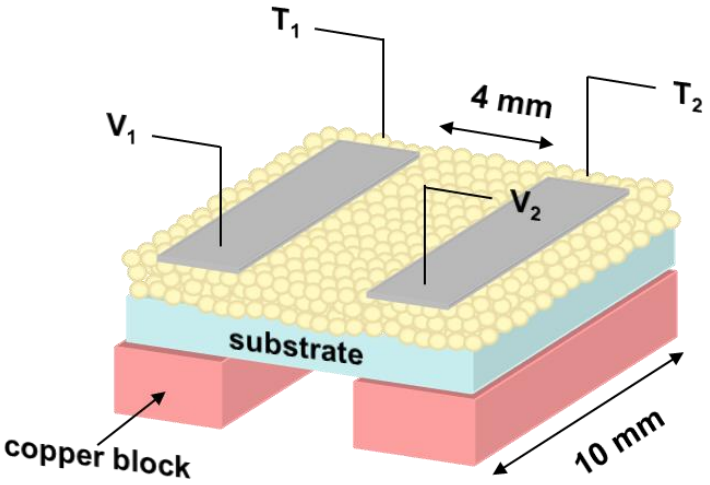

Figure 2.2 Schematic of the samples for thermopower measurement. T_1 and T_2 are attached to two red copper blocks.

Seebeck coefficient measurement: As shown in Figure 2.2, the temperatures of two blocks (T_1 and T_2) were measured and controlled by Lakeshore 336 temperature controller. The voltage of two blocks (V_1 and V_2) were measured by Keithley 617 source measuring units. Corresponding Seebeck coefficients were calculated by LabVIEW programs according to the equation (3).

$$S = -\frac{V_2 - V_1}{T_2 - T_1} \tag{3}$$

2.3 Results and discussion

2.3.1 Film density study

Table 2.2 shows synthesis parameters for P-doped Si NC films with different Ar flow rates and orifice widths. Compared with sample A, sample B increases Ar flow rate from 50 sccm to 100 sccm. Sample C decreases the orifice width from 0.610 mm to only 0.102 mm, resulting the enhancement of the upstream pressure from 1.03 Torr to 4.21 Torr.

Table 2.2 Synthesis parameters for P-doped Si NC films.

	Ar Flow (sccm)	SiH_4 Flow (sccm)	PH_3 Flow (sccm)	Deposition Time (s)	Upstream Pressure (Torr)	Orifice width (mm)	Mean NC size (nm)
A	50	0.81	0.60	20	1.03	0.610	5.2
B	100	0.81	0.60	60	1.22	0.610	5.2
C	100	0.81	0.60	60	4.21	0.102	8.2

Figure 2.3 shows the cross-sectional SEM images and XRD of sample A, B, and C. SEM w the change of the film morphology and XRD shows the change of average nanocrystal size. Combining Table 2.2 and Figure 2.3, as Ar flow rate increases or orifice width decreases, the upstream pressure increases, resulting in a denser film with larger

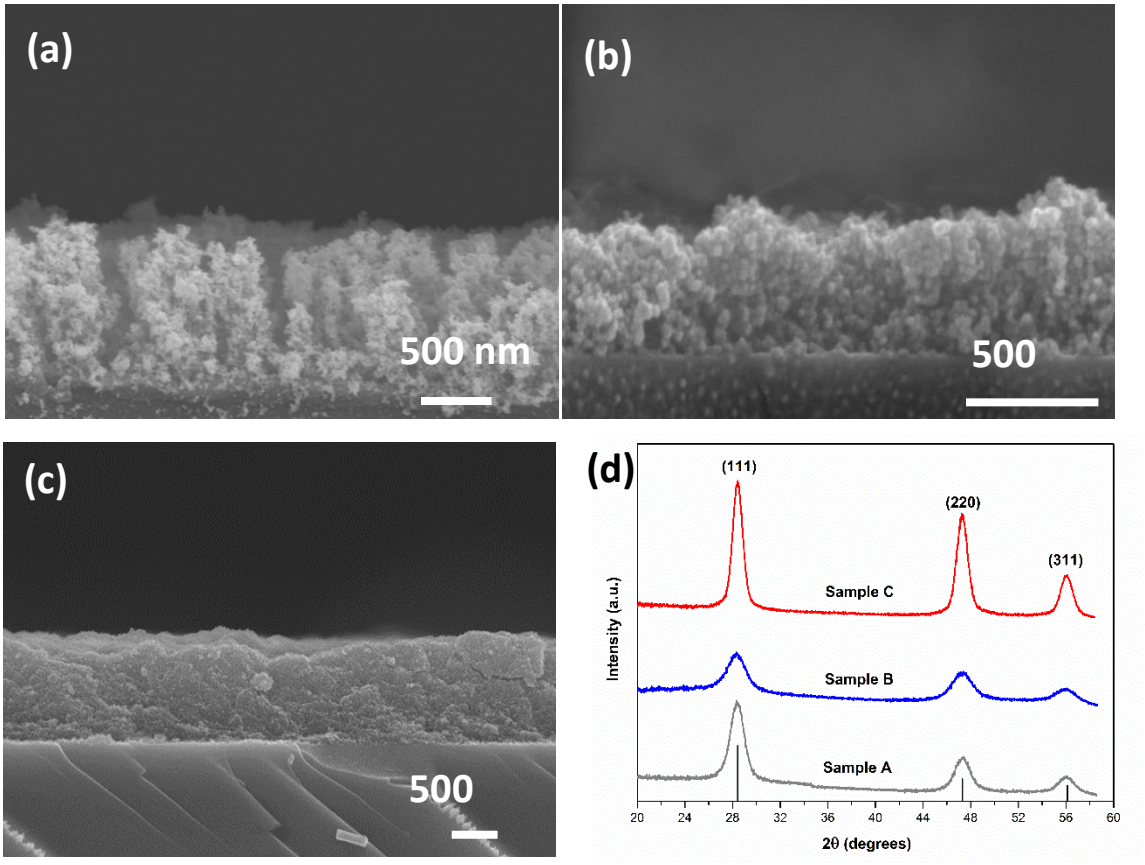

Figure 2.3 Cross-sectional SEM images: (a) Sample A, (b) Sample B, (c) Sample C; (d) XRD images of Sample A, Sample B and Sample C.

nanocrystals. The density of this film is up to 28% according to the spectroscopy ellipsometry.

A simple model for the impaction process in synthesizing NCs from the paper by Holman and Kortshagen in 2010[29] is used to analyze the parameters for the doped Si NCs film. The density of the film is determined by the density of NCs per second and the velocity of NCs arriving the substrate. For the first point, the number of NCs per area per second is related to the reaction rate of NCs in the plasma, which is determined by flow rates of the precursors and the power. However, due to the danger of our precursors, flow rates of them are limited at a low level. For the second point, the velocity of NCs arriving at the substrate is related to both the upstream pressure (P_{up}) and the pressure drop (P_{up}/P_{down}). From the model in Ref 29, gases and NCs are more strongly coupled by increasing P_{up}, resulting in higher velocity of NCs. P_{up} is determined by the flow rate and orifice width. To increase P_{up}, flow rate needs to be increased and orifice width needs to be decreased as shown in Table 2.2.

2.3.2 Effect of different phosphorus doping level

Using the nonthermal plasma reactor shown in Figure 2.1, different phosphorus doping level Si NC films were synthesized with different PH_3 flow rates. The fractional phosphorus atom rate (X_P) defined in equation (4), was used to represent the phosphorus doping level.

$$X_P = \frac{[PH_3]}{[PH_3]+[SiH_4]} \times 100\% \quad (4)$$

Table 2.3 Synthesis parameters for different phosphorus doping level Si NC films.

	Ar Flow (sccm)	SiH_4 Flow (sccm)	PH_3 Flow (sccm)	Upstream Pressure (Torr)	Orifice width (mm)	Mean size of NCs (nm)
undoped Si NC	100	1.14	0.00	4.36	0.102	10.6
10% P-doped Si NC	100	0.81	0.60	4.21	0.102	8.2
30% P-doped Si NC	100	0.84	2.40	4.52	0.102	8.2

$[PH_3]$ is the flow rate of PH_3 and $[SiH_4]$ is the flow rate of SiH_4. For example, 30% P-doped Si NC films means X_P is 30% for these films. Undoped, 10% P-doped, 30% P-doped Si NC films were synthesized with the synthesis parameters in Table 2.3.

Figure 2.4 shows the XRD results of undoped Si NCs, 10% P-doped Si NCs, and 30% P-doped Si NCs. Compared with the standard peaks of silicon single crystals including (111), (220), and (311), all samples are silicon single crystals. The mean size of nanocrystals can

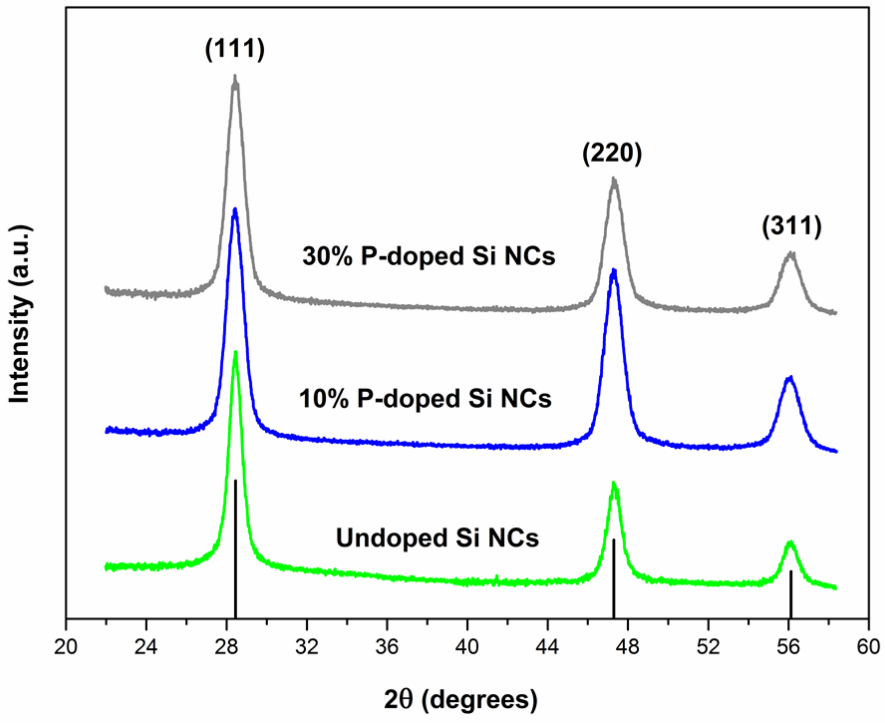

Figure 2.4 XRD of undoped Si NCs, 10% P-doped Si NCs, and 30% P-doped Si NCs.

be calculated from the Scherrer equation and shown in table 2.3.

$$L = \frac{K\lambda}{\beta \cos\theta} \quad (5)$$

L is the mean size of the crystalline. K is a shape factor related to different shape of the crystalline. λ is the X-ray wavelength and θ is the Bragg angle (in degrees). β is the line broadening at half the maximum intensity (FWHM).

Then, two aluminum electrodes were deposited on the sample as shown in Figure 2.2. Electrical conductivities of undoped, 10% P-doped, and 30% P-doped Si NC films were measured in the vacuum chamber from 300 K to 400 K shown in Figure 2.5. At the same temperature, as the phosphorus doping level increases, the electrical conductivity increases due to more free electrons in the film.[31] As the temperature (T) increases, the electrical conductivity (σ) exponent increases according to the Arrhenius equation (6).

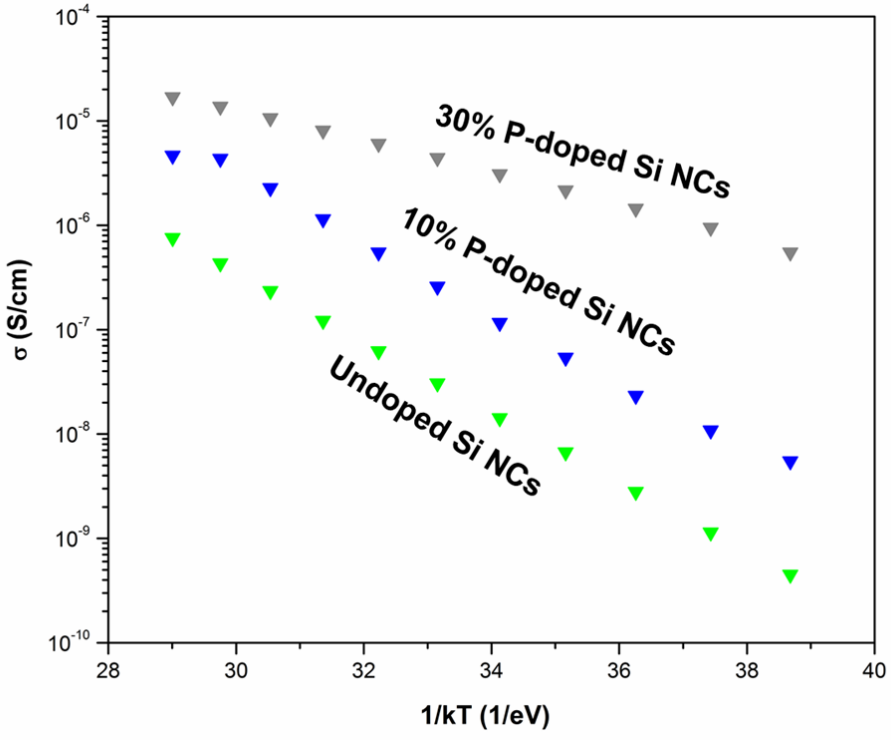

Figure 2.5 Electrical conductivities of undoped Si NC films, 10% P-doped Si NC films, and 30% P-doped Si NC films from 300 K to 400 K.

$$\sigma = \sigma_0 \exp(-\frac{E_a}{kT}) \quad (6)$$

k is Boltzmann constant, which is $1.38064852\times10^{-23}\cdot m^2\cdot kg\cdot s^{-2}\cdot K^{-1}$. E_a is the activation energy, which is transport carriers need to overcome the potential barrier. From the slope of each line in Figure 2.5, the activation energy of the film was calculated and shown in table 2.4. As phosphorus doping level increases, the activation energy of the film decreases.

Table 2.4 Activation energy for different phosphorus doping level Si NC films.

	undoped Si NC	**10% P-doped Si NC**	**30% P-doped Si NC**
Activation energy (eV)	0.334	0.324	0.153

2.3.3 Effect of annealing

There are two annealing methods in this research. One is to anneal the sample on the heater at 450 ˚C for 1 h in the N_2 glovebox. Both the O_2 level and H_2O level in the N_2 glovebox are controlled less than 0.1 ppm. The other is to anneal the sample in the furnace at high temperature from 400 ˚C to 800 ˚C with the N_2 flow rate.

In this chapter, some 10% P-doped Si NC films were annealed on the heater in the N_2 glovebox. Figure 2.6 shows the cross-sectional and surface SEM images of films before and after annealing at 450 ˚C for 1 h. Compared with as-produced films, films after annealing do not change a lot. The thicknesses of them are both around 1 μm.

Figure 2.7 shows electrical conductivities of undoped Si NC films and 10% doped Si NC films before and after annealing at 450 °C for 1 h in the N_2 glovebox from 300 K to 400 K. At the same temperature, the electrical conductivity of the film increases 10 times after annealing. From the slope of lines, the activation energies of films were calculated and

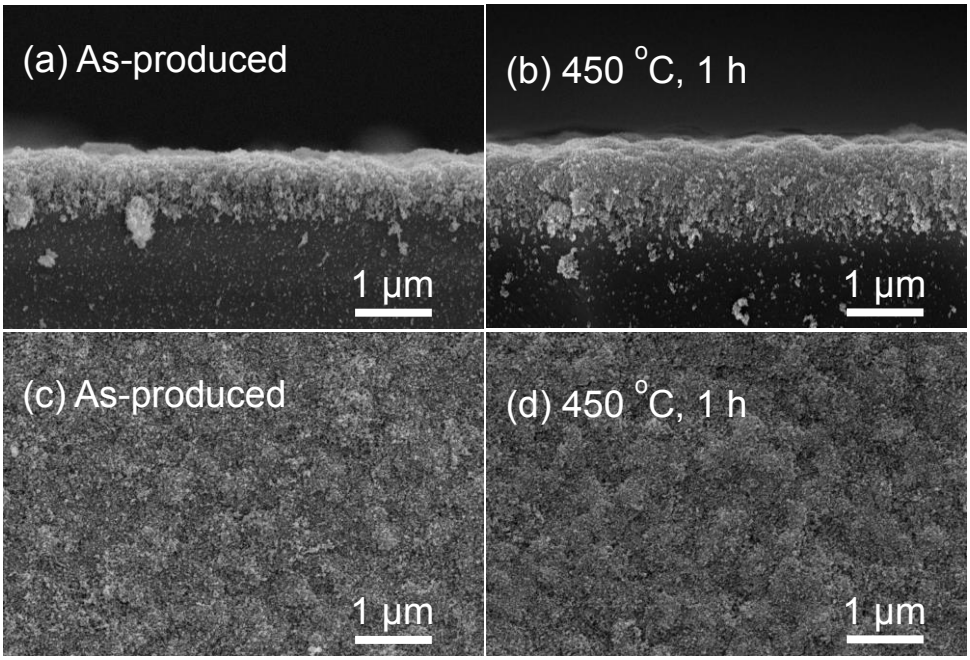

Figure 2.6 SEM images of 10% P-doped Si NC films (a) cross-sectional image of the as-produced film, (b) cross-sectional image of the film after annealing at 450 °C for 1 h, (c) surface image of the as-produced film, (d) surface image of the film after annealing at 450 °C for 1 h.

shown in table 2.5. Activation energies before and after annealing are similar.

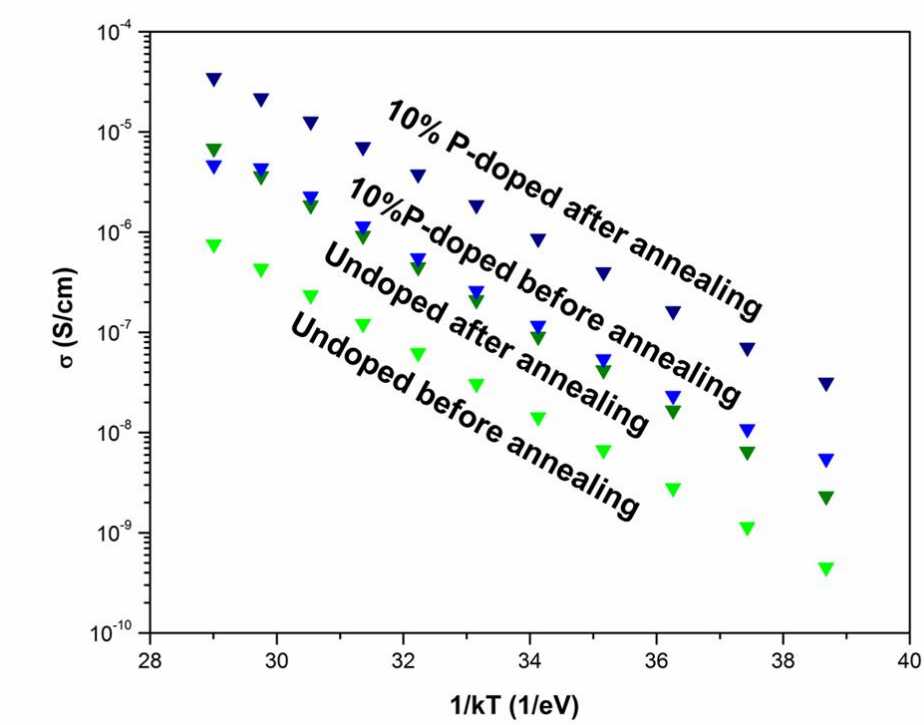

Figure 2.7 Electrical conductivities of undoped Si NC films and 10% P-doped Si NC films before and after annealing at 450 °C for 1 h in the N_2 glovebox from 300 K to 400 K.

Table 2.5 Activation energy for undoped and 10% doped Si NC films before and after annealing

	undoped Si NC before annealing	**undoped Si NC after annealing**	**10% P-doped Si NC before annealing**	**10% P-doped Si NC after annealing**
Activation energy (eV)	0.334	0.358	0.324	0.322

2.3.4 Effect of thickness

30% P-doped Si NC films with different thickness were synthesized using the same synthesis parameters. From the cross-sectional SEM images in Figure 2.8, the thicknesses of them are 1 μm and 5 μm.

Figure 2.9 (a) shows electrical conductivities of 1 μm and 5 μm 30% P-doped Si NC films. At the same temperature, the electrical conductivity of 5 μm film is higher than 1 μm film. Several reasons can be considered. First, the connection of nanocrystals is better in 5 μm film because it is thicker than 1 μm film. Second, films were oxidized differently before measurements because samples were exposed in the air for several minutes before the electrical conductivity measurement. Figure 2.9 (b) shows Seebeck coefficients of 1

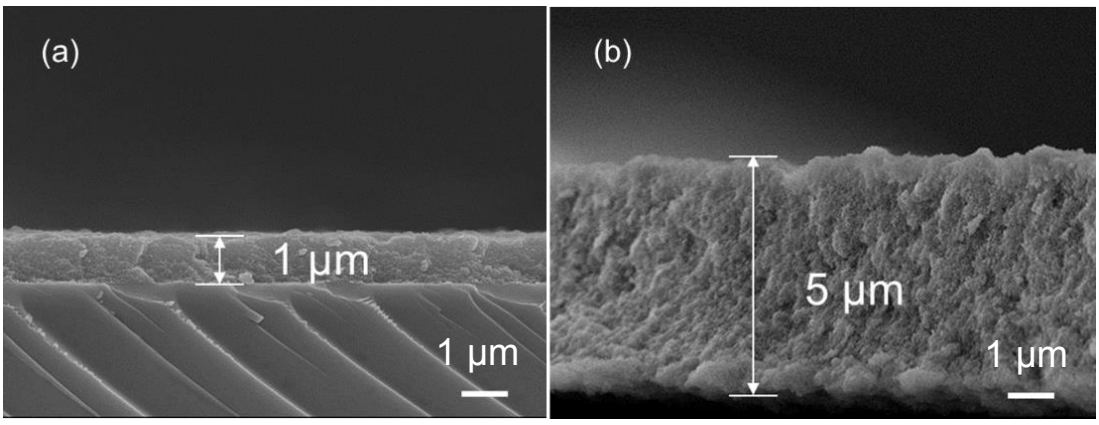

Figure 2.8 Cross-sectional SEM images of 30% P-doped Si NC films (a) the thickness is around 1 μm, (b) the thickness is around 5 μm.

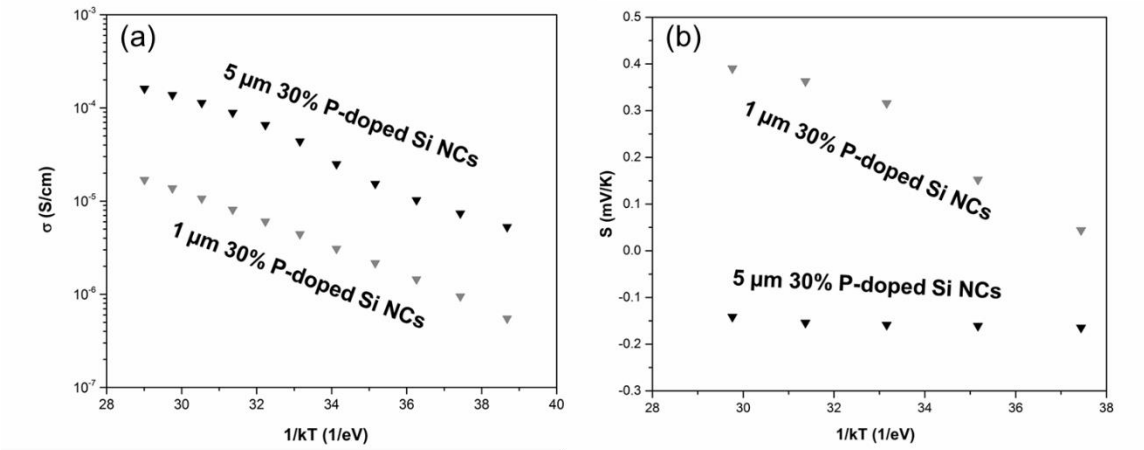

Figure 2.9 30% P-doped Si NC films (a) electrical conductivities of 1 μm and 5 μm films from 300 K to 400 K, (b) Seebeck coefficient of 1 μm and 5 μm films from 300 K to 400 K.

μm and 5 μm 30% P-doped Si NC films. An interesting phenomenon was found in 1 μm 30% P-doped Si NC films. Its Seebeck coefficients are positive, which means main carriers in this film are holes according to the introduction part and equation (3). However, for P-doped Si NC films, main carriers should be electrons. For 5 μm 30% P-doped Si NC films, Seebeck coefficients are negative, which is normal for N-type materials. This interesting phenomenon was thought to be related to the oxidation process before the Seebeck coefficient measurement. More studies were done on the effect of oxidation in the next part.

2.3.5 Effect of oxidation

5 μm 30% P-doped Si NC films were synthesized and moved to the vacuum chamber to measure the electrical conductivity and the Seebeck coefficient from 300 K to 400 K. Then, the same sample was exposed in the air for 5 minutes, 30 minutes, an hour, a day, and a week. After the oxidation, electrical conductivities and Seebeck coefficients of it were measured in the vacuum chamber again.

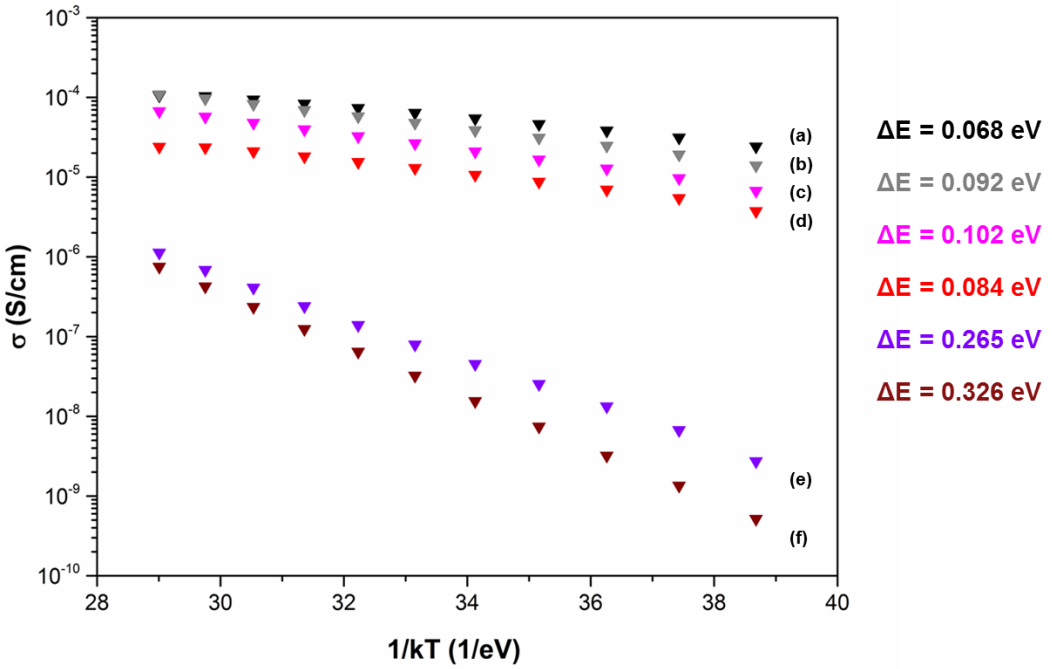

Figure 2.10 Electrical conductivity of 5 μm 30% P-doped Si NC films from 300 K to 400 K (a) as-produced, (b) after 5 minutes oxidation, (c) after 30 minutes oxidation, (d) after an hour oxidation, (e) after a day oxidation, (f) after a week oxidation.

Figure 2.10 shows electrical conductivities of films from 300 K to 400 K. From (a) to (f), as the oxidation time for the same film increases from 5 minutes to a week, the electrical conductivity decreases at the same temperature, and the slope of each line increases, representing the increasing of the activation energy. The activation energies of the sample after different oxidation time were calculated and shown in Figure 2.10.

Figure 2.11 shows Seebeck coefficients of films from 300 K to 400 K. Also, from (a) to (f), the oxidation time increases from 5 minutes to a week. An interesting and amazing phenomenon was found. Seebeck coefficients of the film after 5 minutes oxidation (b) are similar to those of the as-produced film (a) at different temperatures. All of them are negative, which means main carriers are electrons. As the oxidation time increases continuously, Seebeck coefficients increases apparently at higher temperatures, while

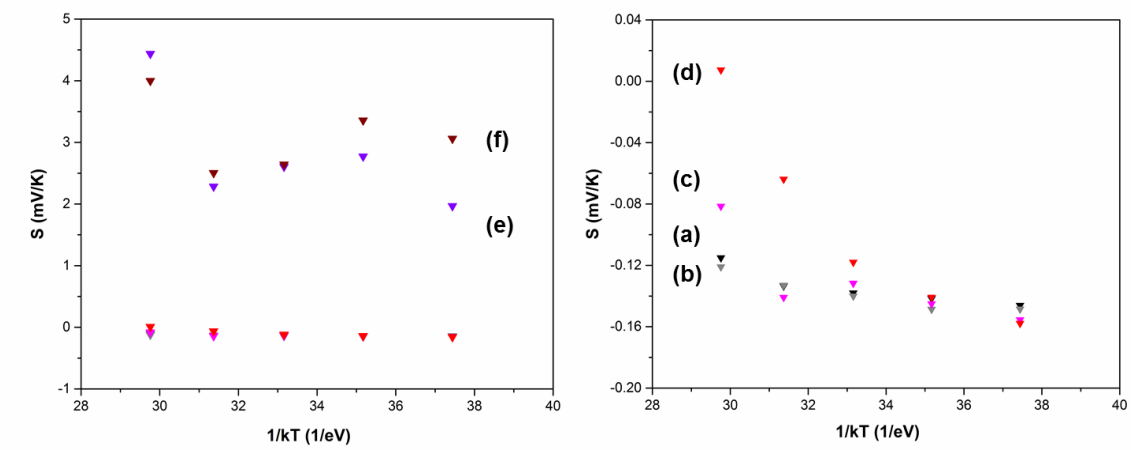

Figure 2.11 Seebeck coefficient of 5 μm 30% P-doped Si NC films from 300 K to 400 K (a) as-produced, (b) after 5 minutes oxidation, (c) after 30 minutes oxidation, (d) after an hour oxidation, (e) after a day oxidation, (f) after a week oxidation.

Seebeck coefficients are closed at low temperatures. The Seebeck coefficient of the film after an hour oxidation first time transfers from negative to positive when the temperature is around 390 K, which means main carriers in this film change from electrons to holes. When the oxidation time is larger than one day, the Seebeck coefficient becomes positive at all temperatures. This oxidation effect can explain positive Seebeck coefficients in 30% P-doped Si NC films with 1 μm thickness, while negative Seebeck coeffients in the same films with 5 μm thickness. The probable mechanism for this abnormal behavior is still unclear. More studies need to be done.

2.4 Conclusion

The density of P-doped Si NC films can be improved when the flow rate increases and the orifice width decreases. As the phosphorus doping level increases, the electrical conductivity increases, and the activation energies decreases. Annealing can improve the electrical conductivities 10 times but have little effect on activation energies. Electrical

conductivities and Seebeck coefficient of films with different thickness are different probably due to the different oxidation levels for them. The oxidation layer traps free electrons, resulting in the decrease of electrical conductivities, the increase of the activation energy, and the transfer of Seebeck coefficient from negative to positive.

3. B-doped silicon nanocrystal films

3.1 Background

In this chapter, some study of thermoelectrical properties of B-doped Si NCs are described. First, the effect of different boron doping level on electrical conductivities of films from 300 K to 400 K was studied. Then, the effect of annealing in the furnace on the film was found. Finally, the oxidation effect on the electrical conductivity of films was studied.

3.2 Experimental methods

The synthesis method and characterization methods were similar in the last chapter 2.2. The only difference is that B_2H_6 (diluted 15% in H_2) replaced PH_3 (diluted 15% in H_2) to produce B-doped Si NC films.

Fourier-transform infrared spectroscopy (FTIR): Nicolet Series II Magna-IR System 750 FTIR was used to measure the absorption of beam from 9600 – 350 cm^{-1}.

Annealing in the furnace: Samples were annealed in the furnace at high temperature from 400 °C to 800 °C with the N_2 flow rate.

3.3 Results and discussion

3.3.1 Effect of different boron doping level

10% B-doped Si NC films were first synthesized using the nonthermal plasma reactor shown in Figure 2.1. The fractional boron rate (X_B) defined in equation (7), was used to represent the boron doping level.

$$X_B = \frac{2[B_2H_6]}{2[B_2H_6]+[SiH_4]} \times 100\% \quad (7)$$

$[B_2H_6]$ is the flow rate of B_2H_6 and $[SiH_4]$ is the flow rate of SiH_4. 10% B-doped Si NC films means X_B is 10% for these films. Synthesis parameters for these films were shown in Table 3.1.

Figure 3.1(a)-(c) show the cross-sectional SEM images of 10% B-doped Si NC film. The film is dense and consists of nanocrystals. The thickness is around 1.2 μm. Figure 3.1 (d)

Table 3.1 Synthesis parameters for 10% B-doped Si NC films.

Ar Flow (sccm)	**SiH_4 Flow (sccm)**	**B_2H_6 Flow (sccm)**	**Power (W)**	**Deposition Time (s)**	**Upstream Pressure (Torr)**	**Orifice width (mm)**
100	1.14	0.64	110	60	4.62	0.102

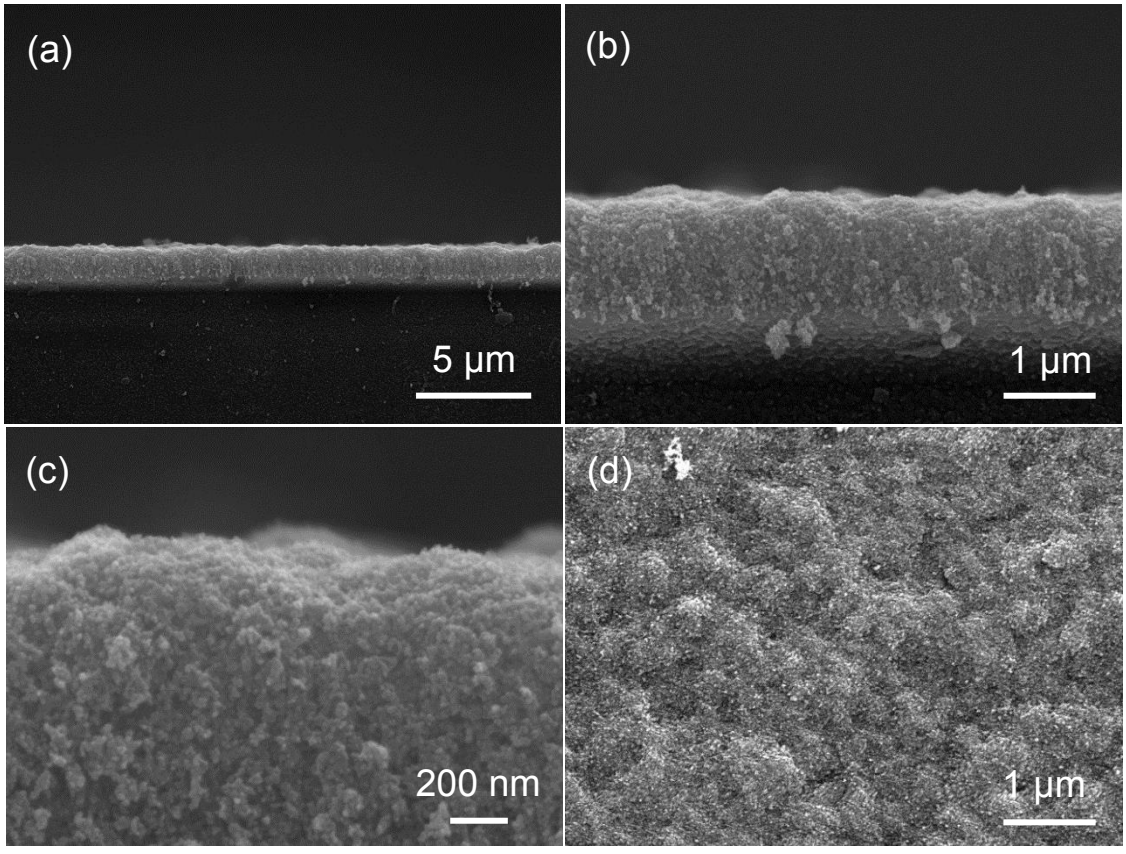

Figure 3.1 SEM images of 10% B-doped Si NC films (a) cross-sectional, 10000 times, (b) cross-sectional, 20000 times, (c) cross-sectional, 60000 times, (d) surface, 20000 times.

shows the surface SEM image of 10% B-doped Si NC films. The morphology of 5% B-doped, 0.5% B-doped, undoped Si NC films are similar. The synthesis parameters for these films were shown in Table 3.2.

Figure 3.2 shows the XRD results for undoped Si NCs and different boron doping level Si NCs. Compared with standard peaks for silicon single crystals, all these samples consist of

Table 3.2 Synthesis parameters for different boron doping level Si NC films.

	Ar Flow (sccm)	**SiH_4 Flow (sccm)**	**B_2H_6 Flow (sccm)**	**Upstream Pressure (Torr)**	**Orifice width (mm)**
undoped Si NC	100	1.14	0.00	4.36	0.102
0.5% B-doped Si NC	100	1.14	using tank	4.16	0.102
5% P-doped Si NC	100	1.14	0.30	4.47	0.102

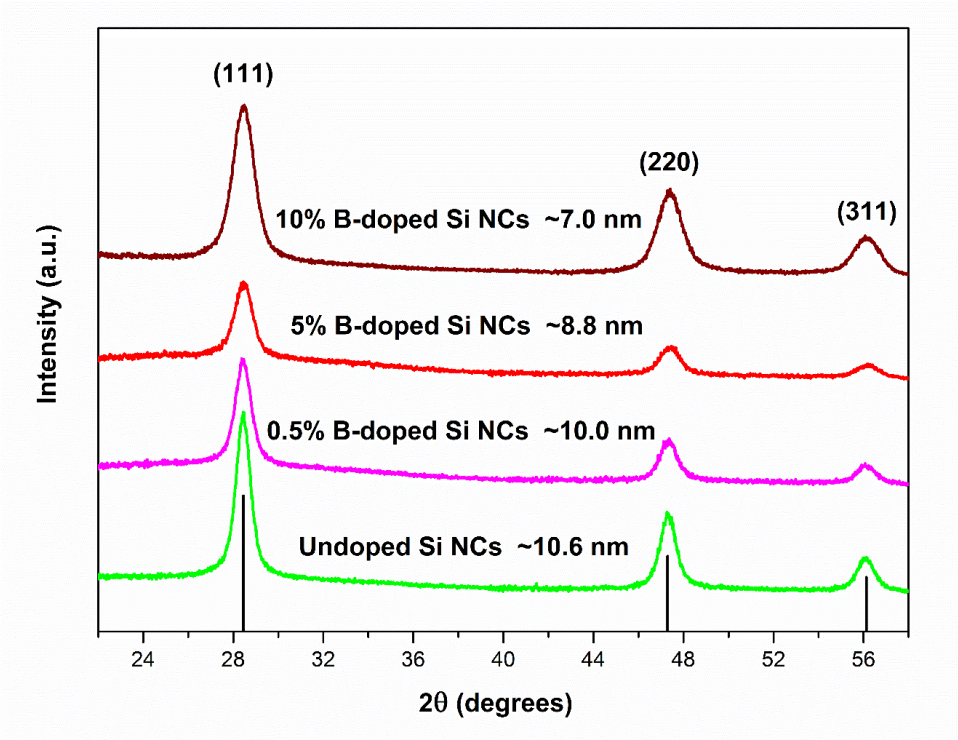

Figure 3.2 XRD of undoped Si NCs, 0.5% B-doped Si NCs, 5% B-doped Si NCs and 10% B-doped Si NCs.

single crystal particles. From the Scherrer equation, equation (5), the mean size of nanocrystals in each film can be calculated and were shown in Figure 3.2. As the boron doping level increases, the mean size of nanocrystals decreases. The reason is that the diborane gas for boron doping was 10% diluted in the hydrogen gas. As diborane gas flow rate increased, the hydrogen gas also increased. There is a balance between the diborane, boron, and hydrogen from the equation (8).

$$B_2H_6 \leftrightarrow 2B + 3H_2 \quad (8)$$

As the hydrogen concentration increases, some boron atoms at the surface will be etched to form diborane again.[27] Therefore, the mean size of nanocrystals decreases when diborane flow rate increases. The similar phenomenon was found in P-doped Si NCs from many experimental results, although the average size of 10% P-doped Si NCs is the same as that of 30% P-doped Si NCs from table 2.3 according to Figure 2.4.

Electrical conductivities of undoped, 0.5% B-doped, 5% B-doped and 10% B-doped Si NC films were measured in the vacuum chamber from 300 K to 400 K shown in Figure 3.3. As the boron doping level increases, the electrical conductivity increases due to more free holes in the film.[31] The relationship between the electrical conductivity and temperature satisfies the Arrhenius equation, equation (6). From the slope of lines, the activation energy was calculated and shown in Table 3.3. The activation energy decreases after boron doping. For so small activation energies close to 0 eV, there are two possible reasons. One is that B-doped films were probably degenerate. Similar results were found in the previously paper.[33] This can be explained that as the number of boron increases in each silicon nanocrystal, activated boron atoms shift the Fermi energy down to the valance band, which means the film becomes a degenerate semiconductor and the electrical conductivities

are independent with temperatures. The other is that in B-doped Si NC films, the transport mechanism is multi-phonon hopping. However, due to the narrow temperature range and big temperature steps, it is hard to find out the transport mechanism. More studies need to be done on this part in the future.

Compared with the similar phosphorus doping level, electrical conductivities of B-doped Si NCs films are higher and activation energies are much smaller. There are two probable reasons. One is the boron doping efficiency is higher than phosphorus doping efficiency. The other is phosphorus atoms are mainly at the surface of silicon nanocrystals, while more boron atoms are at the core.[32] [34] Therefore, there are more activated carriers in boron doped films.

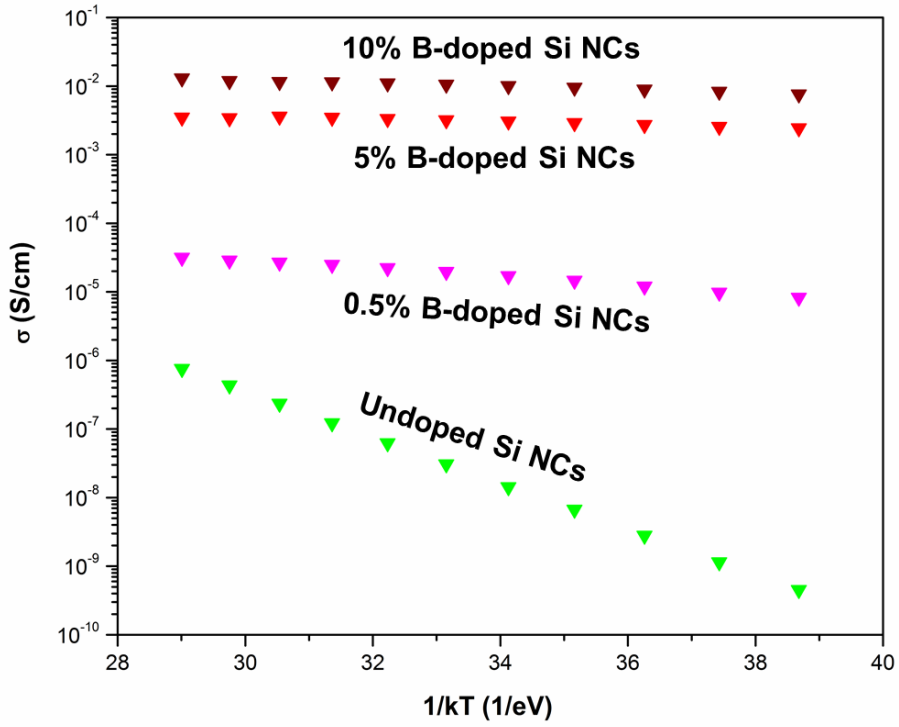

Figure 3.3 Electrical conductivities of undoped Si NC films, 0.5% B-doped Si NC films, 5% B-doped Si NC films and 10% B-doped Si NC films from 300 K to 400 K.

Table 3.3 Activation energy for undoped and B-doped Si NC films.

	undoped Si NC films	**0.5% B-doped Si NC films**	**5% B-doped Si NC films**	**10% B-doped Si NC films**
Activation energy (eV)	0.334	0.061	0.018	0.022

Figure 3.4 (a) shows Seebeck coefficients of 5% B-doped Si NC films and 10% B-doped Si NC films from 300 K to 400 K. All of them are positive, which means main carriers are holes. Seebeck coefficients of 5% B-doped Si NC films are larger than those of 10% B-doepd Si NC films at the same temperature. This is consistent with electrical conductivities of 5% B-doped and 10% B-doped Si NCs. They are probably degenerate. For degenerate semiconductor films, Seebeck coeffificient of them is like that of metal. Films with lighter doping level have lower Seebeck coefficient. Combining Figure 3.3 and Figuere 3.4 (a), power factors (PF = σS^2) of 5% B-doped Si NC films and 10% B-doped Si NC films from 300 K to 400 K can be calculated and shown in Figure 3.4 (b). To calculate the ZT value of films, thermal conductivities of them need to measure. This is what will be done in the future.

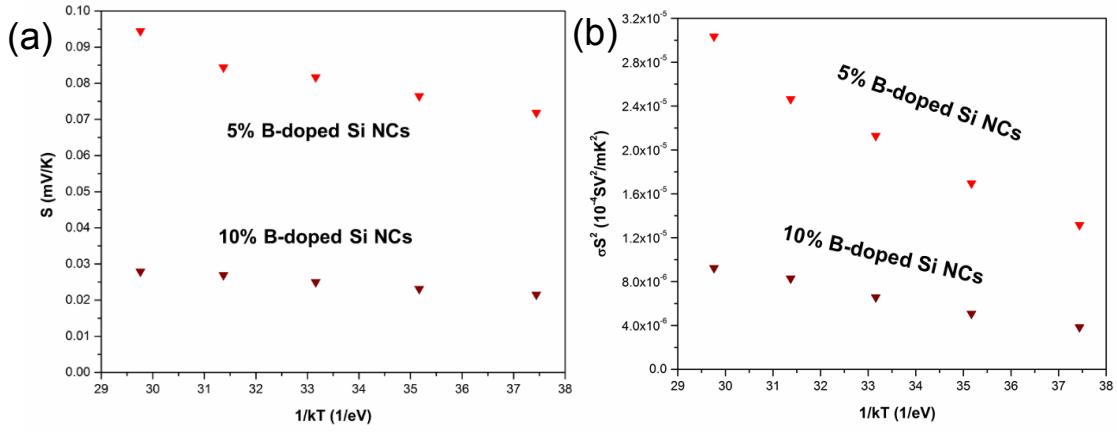

Figure 3.4 (a) Seebeck coefficient of 5% B-doped Si NC films and 10% B-doped Si NC films from 300 K to 400 K, (b) Power factor of 5% B-doped Si NC films and 10% B-doped Si NC films from 300 K to 400 K.

3.3.2 Effect of annealing

In the last chapter, the effect of annealing the sample on the heater in the N2 glovebox was studied for undoped Si NC films and 10% P-doped Si NC films. In this chapter, another annealing method for B-doped Si NC films were discussed. 5% B-doped Si NC films were first synthesized for 5 minutes using the nonthermal plasma reactor in 2.2. Some of them were annealed in the furnace with N_2 flow rate from 400 °C to 800 °C.

Figure 3.5 (a)-(c) show the cross-sectional SEM images of some samples before and after annealing. From Figure 3.5 (a), the thickness of as-produced film is around 5 μm. Figure

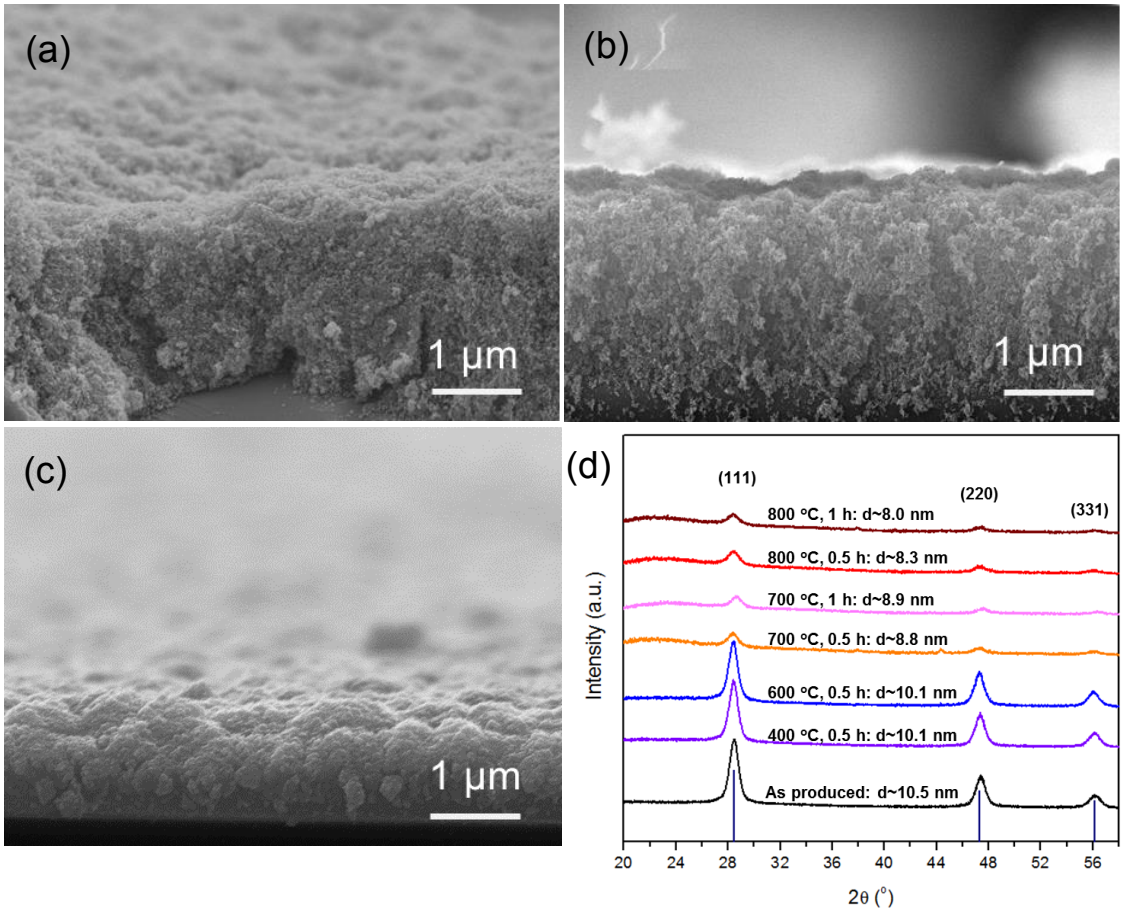

Figure 3.5 5% B-doped Si NC films (a) cross-sectional SEM image of as-produced films, (b) cross-sectional SEM image of films after annealing at 600 °C for 0.5 h, (c) cross-sectional SEM image of films after annealing at 800 °C for 0.5 h, (d) XRD for as-produced films and films after annealing in the furnace from 400 °C to 800 °C.

3.5 (b) is from the sample after annealing in the furnace at 600 °C for 0.5 h. It looks similar with the as-produced film and the thickness is still around 5 μm. When the annealing temperature is up to 800 °C, the sample looks like Figure 3.5 (c). Nanocrystals in the film accumulated together and thickness of the film decreased to only 1 μm. Some nanocrystals were annealed and sublimated during the process.

Figure 3.5 (d) shows XRD results for as-produced films and films after annealing in the furnace from 400 °C to 800 °C. As annealing temperature increases, the peak intensities of the sample decreases, especially, when temperature is higher than 700 °C. The thickness of films decreased a lot after annealing at the temperature over 700 °C, which is consistent with SEM images. From the Scherrer equation, equation (5), the mean size of nanocrystals can be calculated. It decreases as the annealing temperature increases.

Then, resistances of 5% B-doped Si NC films before and after annealing in the furnace from 400 °C to 800 °C were measured in the vacuum chamber at the room temperature and shown in Table 3.4. After annealing, the resistance decreases rather than increases. Two possible reasons were come up with. First, boron doping level decreases due to the form of B_2H_6 gas during the annealing process, which is consistent with SEM and XRD results. Second, oxidation layer was formed during the annealing process. Although N_2 flow rate passed through the furnace, oxygen was not eliminated completely. Oxidation layer can increase the resistance because silicon oxide is insulated.

Table 3.4 Resistances of 5% B-doped Si NC films before and after annealing from 400 °C to 800 °C.

Films	**As produced**	**400** °C, 0.5 h	**600** °C, 0.5 h	**700** °C, 0.5 h	**800** °C, 0.5 h	**800** °C, 1 h
Resistance	$\sim10^5$ Ω	$\sim10^7$ Ω	$\sim10^7$ Ω	$\sim10^{10}$ Ω	$\sim10^{14}$ Ω	$\sim10^{14}$ Ω

3.3.3 Effect of oxidation

To study the effect of oxidation on B-doped Si NC films, 5% B-doped Si NC films were synthesized and exposed in the air for different time. Figure 3.6 shows FTIR results of 5% B-doped Si NC films after oxidation in the air from 5 minutes to a day. From the intensity of the Si-O-Si peak, the oxidation happened. The oxidation process can be explained with the Cabrera-Mott mechanism.[35] During the oxidation, an oxide shell covers Si NC at the surface. Electrons can pass freely from the core to the oxide surface to ionize oxygen atoms. This also results in an electric field that points from the core toward the surface. Oxygen ions can diffuse and oxidize Si NCs in the core under the electric field. Phosphorus doping

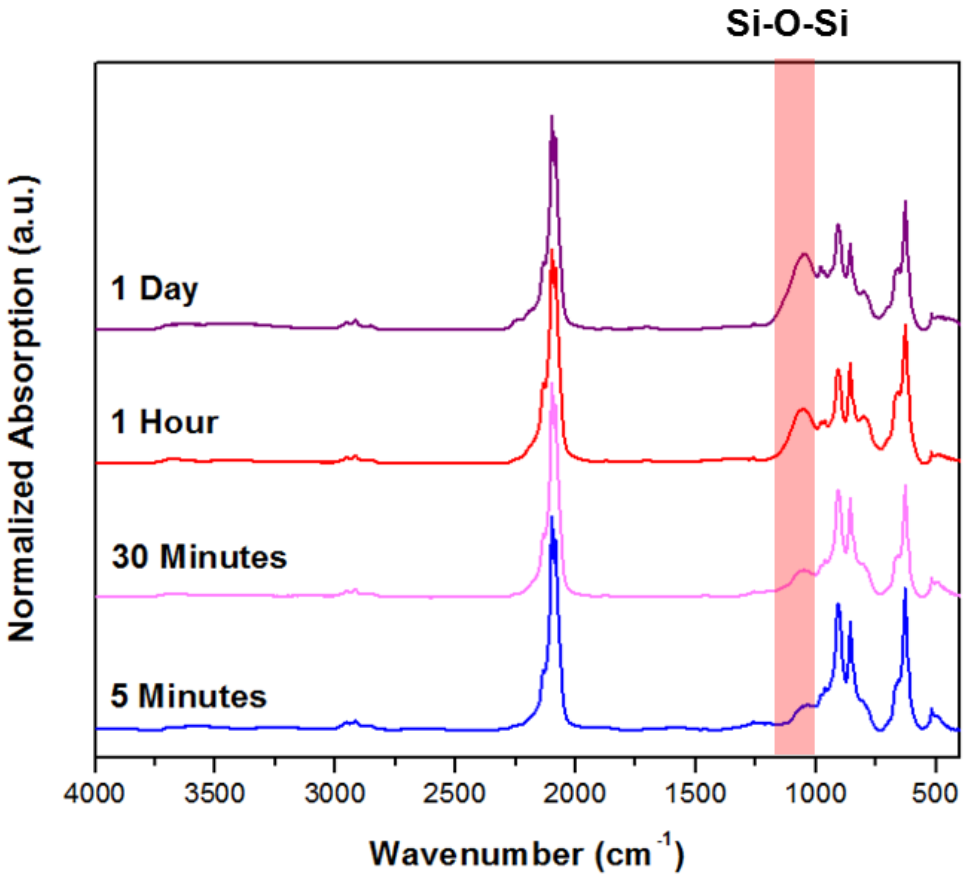

Figure 3.6 FTIR for 5% B-doped Si NC films after oxidation for different time from 5 minutes to a dav.

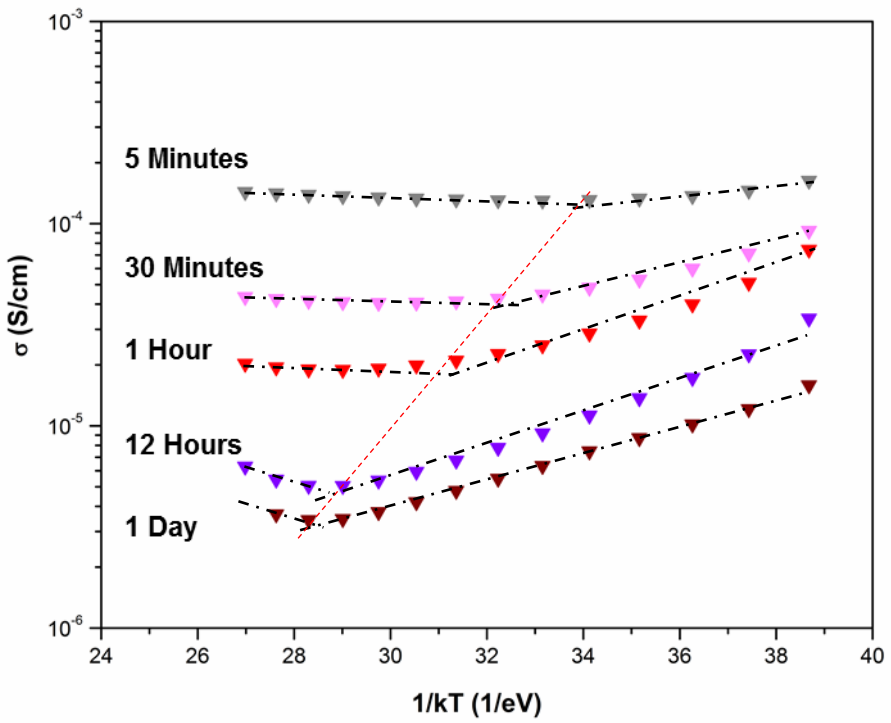

Figure 3.7 Electrical conductivities of 5% B-doped Si NC films after oxidation for different time from 5 minutes to a dav.

increases the speed of the oxidation because the tunneling of P induces free electrons to enhance the electric field. While boron doping weakens the speed of the oxidation.[34]

The effect of oxidation on electrical conductivities of 5% B-doped Si NC films is shown in Figure 3.7. After oxidation, the electrical conductivity of films decreases at the same temperature. For a fixed oxidation time, an abnormal phenomenon is found that as the high temperature, the electrical conductivity decreases as temperature decreases, while at the low temperature, the electrical conductivities increases as the temperature decreases. There is a transition point between the 300 K and 430 K. As the oxidation time increases, the transition point moves from 340K to 400 K. This is much more like the metal-insulator transition in the metal. The similar behavior was found in P-type Si:B samples at very low

temperatures (55 mK to 4.2 K).[33] To learn more about the transport mechanism for B-doped Si NC films after oxidation, more studies need to be done.

3.4 Conclusion

The effect of different boron doping level on Si NC films was studied. As the boron doping level increased, the mean size of NCs decreased due to the H2 etching. The electrical conductivity of the film increased several orders and the activation energy decreased probably because the film was degenerately doped. But doping was not good for the enhancement of Seebeck coefficients. Annealing in the furnace increased the resistance of films, especially when annealing temperature was over 700 °C. The effect of the oxidation on electrical conductivities were complicated. It appeared a transition point after the oxidation. To learn more about the transport mechanism for B-doped Si NC films, more electrical conductivities in a wider range of temperatures need to be measured.

4. Summary and proposed work

Studying high-performance and inexpensive thermoelectric materials to transfer the thermal energy to electrical energy is significant. Silicon is a low cost and widely used semiconductor material. To increase electrical conductivities and decrease thermal conductivities, doped nanostructured silicon has been studied and caught much attention in the past 20 years.

In this research, phosphorus doped and boron doped silicon nanocrystal films was synthesized using nonthermal plasma because of the low air temperature, high-purity nanocrystals, narrow nanocrystal size distribution, and controllable and efficient doping in this method. First, the synthesis parameters for dense films were studied. To obtain dense films, high argon flow rate and small orifice width were used. SEM, XRD, and Spectroscopy Ellipsometry were used to characterize films. Then, effects of the phosphorus doping level, the thickness, and the oxidation on electrical conductivities and Seebeck coefficients of films were studied. Phosphorus doping can increase electrical conductivities and decrease the activation energy of films fitting the Arrhenius expression. Annealing can increase the electrical conductivities 10 times but cannot affect the activation energy a lot. The electrical conductivities and Seebeck coefficients of films with defferent thicknesses are different due to the different oxidation level. The oxidation decreases electrical conductivities and increases activation energies of films through electron traps at the surface. This also explains an abnormal phenomenon that Seebeck coefficient transfer from negative to positive during the oxidation. Finally, for boron doped silicon nanocrystal films, effects of the doping level, annealing in the furnace, and the oxidation on the electrical conductivities and Seebeck coefficients were studied. Boron doping can decrease the

activation energy of films a lot and probably form the degenerate semiconductor films. But annealing in the furnace cannot improve the electrical conductivities of films probably due to the oxidation and the lose of boron atoms. A transition point for electrical conductivities of films appeared after the oxidation. More studies need to do to find the transport mechanism for this phenomenon.

To obtain ZT value of doped silicon nanocrystal films, thermal conductivities of films need to be measured in the next step. Then, these films can be compared with other thermoelectrical materials. To study transport mechanism for B-doped silicon nanocrystal films, electrical conductivities of films should be measured with narrow steps in a wider temperature range. Then, the Zabrodskii plots can be used to find out the transport mechanism in these films. After that, the effect of the oxidation on electrical conductivities and Seebeck coefficients can be understood more profoundly.

5. Bibliography

1. Biswas, Kanishka, Jiaqing He, Ivan D. Blum, Chun-I. Wu, Timothy P. Hogan, David N. Seidman, Vinayak P. Dravid, and Mercouri G. Kanatzidis. "High-performance bulk thermoelectrics with all-scale hierarchical architectures." Nature 489, no. 7416 (2012): 414.

2. Chen, Xin, Pengtao Lin, Kai Zhang, Helmut Baumgart, Brian Geist, and Vladimir Kochergin. "Seebeck Coefficient Enhancement of ALD PbTe/PbSe Nanolaminate Structures Deposited inside Porous Silicon Templates." ECS Journal of Solid State Science and Technology 5, no. 9 (2016): P503-P508.

3. Zuo, Guangzheng, Xianjie Liu, Mats Fahlman, and Martijn Kemerink. "High Seebeck Coefficient in Mixtures of Conjugated Polymers." Advanced Functional Materials (2017).

4. Venkatasubramanian, Rama, Edward Siivola, Thomas Colpitts, and Brooks O'quinn. "Thin-film thermoelectric devices with high room-temperature figures of merit." Nature 413, no. 6856 (2001): 597.

5. He, Ying, Ping Lu, Xun Shi, Fangfang Xu, Tiansong Zhang, Gerald Jeffrey Snyder, Ctirad Uher, and Lidong Chen. "Ultrahigh thermoelectric performance in mosaic crystals." Advanced Materials 27, no. 24 (2015): 3639-3644.

6. Uher, C. "Recent trends in thermoelectric materials research I." Semiconductors and semimetals 69 (2001): 139-253.

7. Kauzlarich, Susan M., Shawna R. Brown, and G. Jeffrey Snyder. "Zintl phases for thermoelectric devices." Dalton Transactions 21 (2007): 2099-2107.

8. Kleinke, Holger. "New bulk materials for thermoelectric power generation: clathrates and complex antimonides." Chemistry of materials 22, no. 3 (2009): 604-611.

9. Heikes, Robert R., and Roland W. Ure. Thermoelectricity: science and engineering. Interscience Publishers, 1961.

10. Touloukian, Y. S., R. W. Powell, C. Y. Ho, and P. G. Klemens. Thermophysical properties of matter-the tprc data series. volume 1. thermal conductivity-metallic elements and alloys. THERMOPHYSICAL AND ELECTRONIC PROPERTIES INFORMATION ANALYSIS CENTER LAFAYETTE IN, 1970.

11. Weber, L., and E. Gmelin. "Transport properties of silicon." Applied Physics A 53, no. 2 (1991): 136-140.

12. Hicks, L. D., and Mildred S. Dresselhaus. "Effect of quantum-well structures on the thermoelectric figure of merit." Physical Review B 47, no. 19 (1993): 12727.

13. Boukai, Akram I., Yuri Bunimovich, Jamil Tahir-Kheli, Jen-Kan Yu, William A. Goddard Iii, and James R. Heath. "Silicon nanowires as efficient thermoelectric materials." Nature 451, no. 7175 (2008): 168.

14. Hochbaum, Allon I., Renkun Chen, Raul Diaz Delgado, Wenjie Liang, Erik C. Garnett, Mark Najarian, Arun Majumdar, and Peidong Yang. "Enhanced thermoelectric performance of rough silicon nanowires." Nature 451, no. 7175 (2008): 163.

15. Song, David, and Gang Chen. "Thermal conductivity of periodic microporous silicon films." Applied physics letters 84, no. 5 (2004): 687-689.

16. Lee, Joo-Hyoung, Giulia A. Galli, and Jeffrey C. Grossman. "Nanoporous Si as an efficient thermoelectric material." Nano letters 8, no. 11 (2008): 3750-3754.

17. Tang, Jinyao, Hung-Ta Wang, Dong Hyun Lee, Melissa Fardy, Ziyang Huo, Thomas P. Russell, and Peidong Yang. "Holey silicon as an efficient thermoelectric material." Nano letters 10, no. 10 (2010): 4279-4283.

18. Krali, Emiljana, and Zahid AK Durrani. "Seebeck coefficient in silicon nanowire arrays." Applied Physics Letters 102, no. 14 (2013): 143102.

19. Martín-Palma, R. J., H. Cabrera, B. Martín-Adrados, D. Korte, E. Pérez-Cappe, Y. Mosqueda, M. A. Frutis, and E. Danguillecourt. "Thermoelectric properties of nanostructured porous silicon." Materials Research Express 5, no. 1 (2018): 015004.

20. Hashimoto, S., S. Asada, T. Xu, S. Oba, Y. Himeda, R. Yamato, T. Matsukawa, T. Matsuki, and T. Watanabe. "Anomalous Seebeck coefficient observed in silicon nanowire micro thermoelectric generator." Applied Physics Letters 111, no. 2 (2017): 023105.

21. Majumdar, Arun. "Thermoelectricity in semiconductor nanostructures." Science 303, no. 5659 (2004): 777-778.

22. Valalaki, Katerina, Philippe Benech, and Androula Galiouna Nassiopoulou. "High Seebeck Coefficient of Porous Silicon: Study of the Porosity Dependence." Nanoscale research letters 11, no. 1 (2016): 201.

23. Littau, K. A., P. J. Szajowski, A. J. Muller, A. R. Kortan, and L. E. Brus. "A luminescent silicon nanocrystal colloid via a high-temperature aerosol reaction." The Journal of Physical Chemistry 97, no. 6 (1993): 1224-1230.

24. Ehbrecht, Markus, and Friedrich Huisken. "Gas-phase characterization of silicon nanoclusters produced by laser pyrolysis of silane." Physical Review B 59, no. 4 (1999): 2975.

25. Loureiro, Joana, Tiago Mateus, Sergej Filonovich, Marisa Ferreira, Joana Figueira, Alexandra Rodrigues, Brian F. Donovan, Patrick E. Hopkins, and Isabel Ferreira.

"Improved thermoelectric properties of nanocrystalline hydrogenated silicon thin films by post-deposition thermal annealing." Thin Solid Films 642 (2017): 276-280.

26. Mangolini, L., E. Thimsen, and Uwe Kortshagen. "High-yield plasma synthesis of luminescent silicon nanocrystals." Nano letters 5, no. 4 (2005): 655-659.

27. Kortshagen, Uwe R., R. Mohan Sankaran, Rui N. Pereira, Steven L. Girshick, Jeslin J. Wu, and Eray S. Aydil. "Nonthermal plasma synthesis of nanocrystals: fundamental principles, materials, and applications." Chemical reviews 116, no. 18 (2016): 11061-11127.

28. Gorla, C. R., S. Liang, G. S. Tompa, W. E. Mayo, and Y. Lu. "Silicon and germanium nanoparticle formation in an inductively coupled plasma reactor." Journal of Vacuum Science & Technology A: Vacuum, Surfaces, and Films 15, no. 3 (1997): 860-864.

29. Holman, Zachary C., and Uwe R. Kortshagen. "A flexible method for depositing dense nanocrystal thin films: impaction of germanium nanocrystals." Nanotechnology 21, no. 33 (2010): 335302.

30. Rowe, David J. "Impurities in Silicon Nanocrystals: The intentional and the inherent." PhD diss., University of Minnesota, 2013.

31. Sze, S. M. and K. K. Ng. Physics of Semiconductor Devices, 3rd ed. Hoboken, NJ: John Wiley and Sons, 2007.

32. Kramer, Nicolaas J., Katelyn S. Schramke, and Uwe R. Kortshagen. "Plasmonic properties of silicon nanocrystals doped with boron and phosphorus." Nano letters 15, no. 8 (2015): 5597-5603.

33. Dai, Peihua, Youzhu Zhang, and M. P. Sarachik. "Electrical conductivity of metallic Si: B near the metal-insulator transition." Physical Review B 45, no. 8 (1992): 3984.

34. Pi, X. D., R. Gresback, R. W. Liptak, S. A. Campbell, and U. Kortshagen. "Doping efficiency, dopant location, and oxidation of Si nanocrystals." Applied Physics Letters 92, no. 12 (2008): 123102.

35. Cabrera, N. F. M. N., and Nevill Francis Mott. "Theory of the oxidation of metals." Reports on progress in physics 12, no. 1 (1949): 163.